Total Solar Irradiance during the Last Five Centuries

Valentina Penza [ID],[1] Francesco Berrilli [ID],[1] Luca Bertello [ID],[2] Matteo Cantoresi [ID],[1] Serena Criscuoli [ID],[2]
and Piermarco Giobbi [ID][1]

[1]*Dipartimento di Fisica, Università di Roma Tor Vergata, Via della Ricerca Scientifica 1, Roma, 00133, Italy*
[2]*National Solar Observatory, 3665 Discovery Dr., Boulder, CO 80303, USA*

ABSTRACT

The total solar irradiance (TSI) varies on timescales of minute to centuries. On short timescales it varies due to the superposition of intensity fluctuations produced by turbulent convection and acoustic oscillations. On longer scale times, it changes due to photospheric magnetic activity, mainly because of the facular brightenings and dimmings caused by sunspots. While modern TSI variations have been monitored from space since 1970s, TSI variations over much longer periods can only be estimated using either historical observations of magnetic features, possibly supported by flux transport models, or from the measurements of the cosmogenic isotope (e.g., ^{14}C or ^{10}Be) concentrations in tree rings and ice cores. The reconstruction of the TSI in the last few centuries, particularly in the 17th/18th centuries during the Maunder minimum, is of primary importance for studying climatic effects. To separate the temporal components of the irradiance variations, specifically the magnetic cycle from secular variability, we decomposed the signals associated with historical observations of magnetic features and the solar modulation potential Φ by applying an Empirical Mode Decomposition algorithm. Thus, the reconstruction is empirical and does not require any feature contrast or field transport model. The assessed difference between the mean value during the Maunder minimum and the present value is $\simeq 2.5 W m^{-2}$. Moreover it shows, in the first half of the last century, a growth of $\simeq 1.5 W m^{-2}$ which stops around the middle of the century to remain constant for the next 50 years, apart from the modulation due to the solar cycle.

Keywords: solar–terrestrial relations — Sun: activity — Sun: faculae, plages — Sun: sunspots

1. INTRODUCTION

Solar Irradiance is the Earth's primary energy input (Kren et al. 2017) and is a fundamental ingredient for the understanding and characterization of a large variety of phenomena, which include the modeling of terrestrial global or regional climate variations (e.g. Haigh et al. 2010; Lockwood et al. 2010; Lean 2017; Jungclaus et al. 2017; Schmutz 2021), ecosystems (Häder et al. 2011), telecommunications and renewable energies applications (Myers 2017). Recently, a surge in studies of solar irradiance and its variability has been driven by the increasing interest in understanding and modeling the irradiance variability in other stars (Fabbian et al. 2017; Faurobert 2019; Kopp & Shapiro 2021), which, likewise for the Earth, affects exoplanets atmospheres and it is fundamental to assess the climate and habitability of planets orbiting solar-like stars (e.g. Linsky 2019; Galuzzo et al. 2021).

Solar Irradiance is the electromagnetic energy emitted by the Sun in the unit of time and area that fall outside the earth's atmosphere at a distance of one Astronomical Unit. The term Total Solar Irradiance, or TSI, refers to the irradiance integrated over the disk and over the whole energy spectrum. Precise measurements of the TSI have only existed since 1978, as they require the ability to perform observations out of the Earth atmosphere, which absorbs

Corresponding author: Francesco Berrilli
francesco.berrilli@roma2.infn.it

large fractions of the radiation. These observations showed that the TSI varies over time scales from minutes to years and decades (e.g. Woodard & Hudson 1983; Kopp et al. 2016a) and that variations from days to decades are clearly modulated by the solar surface magnetism (Wilson 1978; Hudson 1988). Variations over temporal scales longer than approximately the 11-years solar cycle are difficult to assess, as space missions rarely extend over more than a decade and therefore the creation of long-term irradiance dataset rely on precise intercalibration of measurements obtained with different instruments.

Spurred by the necessity of explaining measured variations on one hand, and producing long records essential to quantify the effects of solar variability on the Earth climate, several models have been developed to reproduce the measured TSI and estimate its variability in the past, before measurements started to be available (e.g. Fröhlich & Lean 2004; Coddington et al. 2016; Tapping et al. 2007; Yeo et al. 2014; Wu et al. 2018). Although often based on very different approaches, all these models take into account mainly the combinations of the effects due to active regions, namely dark sunspots and bright regions network and facular area. It is well known that in this sort of competition, the emission of bright ARs on average exceeds the sunspot deficit, causing a net increase in total irradiance in phase with the magnetic activity level, with a difference between the maximum and minimum of nearly 0.1 %. Models of solar irradiance generally fall into one of two categories: proxy based or semi-empirical.

Proxy models reproduce irradiance variability by regressing irradiance measurements with proxies of magnetic activity. For example, both the Naval Research Laboratory model (NRL, Coddington et al. 2016; Lean et al. 2020) and the EMPirical Irradiance REconstruction (EMPIRE, Yeo et al. 2017) make use of sunspot area and MgII core-to-wing ratio regressed on TSI and SSI measurements to take into account of the sunspot and plage contributions, respectively. In this context, the attempts to reconstruct solar variability also in regions of the spectrum, i.e., ultraviolet, are particularly relevant for the energetic balancing of the earth's upper atmosphere. (e.g. Kutiev et al. 2013; Bordi et al. 2015; Lovric et al. 2017; Criscuoli et al. 2018; Rodriguez et al. 2019; Bertello et al. 2020; Berrilli et al. 2020).

Semi-empirical models, often referred to as physics-based, combine area coverage of quiet and magnetic features, typically derived from full-disk observations, with their corresponding radiative emission. Typically, chromospheric full-disk daily observations, e.g. CaII K index, or coronal observations, are employed in combination with Non Local Thermodynamic Equilibrium (Non-LTE) spectral syntheses obtained with sets of semi-empirically derived atmospheres (e.g. FAL models Fontenla et al. 1999, 2011; Haberreiter 2011; Fontenla et al. 2015) to reproduce both the Total (e.g. Ermolli et al. 2011; Fontenla et al. 2011) and the Spectral Solar Irradiance (Penza et al. 2003; Fontenla et al. 2011; Haberreiter et al. 2014; Fontenla et al. 2017; Criscuoli et al. 2018; Criscuoli 2019). The Spectral and Total Irradiance Reconstructions (SATIRE, Krivova et al. 2007; Ball et al. 2014) makes use of full-disk daily magnetograms to single out magnetic and quiet regions, to which are associated radiative emissions computed under LTE making use of Kurucz and modified FAL models. Typically, irradiance reconstruction models reproduce more than 90% of the observed TSI variability observed at the solar-cycle time scale (e.g. Lean et al. 2020).

Variations over longer temporal scales and their physical origins are still debated. On one hand, as mentioned above assessing these variations through measurements is extremely difficult (e.g. Kopp 2014; Dudok de Wit et al. 2017; Dudok de Wit & Kopp 2020), on the other, different irradiance reconstruction models produce different levels of variability (e.g. Yeo et al. 2017; Lean et al. 2020). From a theoretical perspective, although different mechanisms have been suggested (see for instance the recent reviews by Faurobert 2019; Petrie et al. 2021), the most accepted cause for long-term irradiance variability are variations in the properties of the quiet Sun (e.g. Foukal et al. 2011; Lockwood & Ball 2020). This hypothesis has been recently corroborated by Rempel (2020), who, making use of state-of-the-art magneto hydrodynamic simulations of the solar photosphere, showed that variations as small as 10% of the quiet Sun magnetic properties may induce changes of the TSI amplitude comparable to the 11-years cycle variations. Understanding the properties of the quiet Sun magnetic field and its variations over the solar cycle and longer temporal scales is an active area of research (e.g. Schnerr & Spruit 2011; Criscuoli & Foukal 2017; Faurobert et al. 2020) and is part of the Critical Science Plan (Rast et al. 2021) of the NSF operated Daniel K. Inouye Solar Telescope (Rimmele et al. 2020).

The contribution of quiet Sun to solar irradiance is higher, relatively speaking, during periods of minima. It is known that the solar magnetic activity has crossed grand minima periods, such as the Maunder minimum during the years of 1645 to 1715. Estimate the average level of TSI during these period of minima, and compare it with present measured values, is essential to model natural contributions to the increase of regional or global temperatures observed from the pre-industrial era (e.g. Shindell et al. 2001; Ineson et al. 2015; Jungclaus et al. 2017; Matthes et al. 2017). Models have produced a wide range of possible TSI scenarios for the Maunder minimum, ranging from being comparable (e.g.

Schrijver et al. 2011) to as much as 0.35% (e.g. Egorova et al. 2018) of the current day quiet Sun. The value adopted by the Paleoclimat Modeling Intercomparison Project-4 is 0.055% (Jungclaus et al. 2017), which falls in between the 0.04% and the 0.067% estimated more recently with SATIRE-H (Wu et al. 2018) and NRLTSI-2 (Lean 2018) models, respectively. It is important to note that irradiance reconstructions prior to the twentieth century are necessarily based on the use of proxies, full-disk observations of the Sun being available only starting at the end of the nineteenth century. Two proxies are typically available: sunspot numbers (or groups), dating back to 1610, and radioisotopes, which allow to estimate the solar activity over millennia (Usoskin 2017; Brehm et al. 2021). The models range from using correlation between irradiance and proxies derived from modern observations (Steinhilber et al. 2009; Lean 2018), to the use of models of various degree of complexity to derive the distribution of the magnetic fields over the disk (e.g. Wang et al. 2005; Bolduc et al. 2012; Wu et al. 2018; Berrilli et al. 2020).

In this work we present a novel method to estimate the mean levels of TSI, averaged at 22-y and useful for global or regional climatology studies, and to hypothesize a possible variability of solar magnetic structures, especially sunspots and plage, on a shorter scale, i.e., one year. This method relies on the use of an Empirical Mode Decomposition (EMD) algorithm to separate the different temporal components of the solar activity variability present in the signal of the solar modulation potential Φ to estimate the contribution of sunspot, faculae and quiet magnetic fields to irradiance variability. The Solar modulation potential Φ is defined as the mean energy loss per unit charge by the high-energy charged particles forming the Galactic Cosmic Rays as they propagate through the heliosphere. As discussed in the next section, Φ is modulated by solar activity. EMD is an adaptive and effective algorithm to deal with nonlinear, nonstationary signals and to identify quasi-periodic embedded structures.

2. DATASET AND METHOD

The models that we developed is based on the widely common accepted assumption that on scales from days to the 11-years cycle the TSI is modulated by the positive contribution of faculae (e.g. Pagaran et al. 2009) and network (e.g. Berrilli et al. 1999; Ermolli et al. 2003) and the negative contribution of sunspots (e.g. Wenzler et al. 2006; Ball et al. 2012). Moreover, we assume that variations of the quiet Sun magnetism modulate irradiance at longer temporal scales and that such variations are independent from global dynamo processes. The last assumption is that variations of the solar modulation potential are proxies for the evolution of the solar surface magnetism. This assumption is based on the evidence that solar activity modulates galactic cosmic rays (GCRs) that enter the heliosphere (e.g. Martucci et al. 2018) and that the GCRs modulate some isotopes present in the Earth's atmosphere, e.g., ^{14}C or ^{10}Be. All the assumptions employed in our model are common to other models described in Sec. 1. However, our method differ in the approach employed to estimate the contributions of the different components to the TSI variability from the solar modulation potential. The method, described in detail in the next sections, is briefly summarized here.

We adopted two main composite data sets based on measurements of plages and sunspot areas. Both data sets are publicly available from the Max Plank Institute (MPI) website (http://www2.mps.mpg.de/projects/sun-climate/data.html). The first composite consists of values derived from Ca II K spectroheliogram observations covering the period 1892 to 2019 (Chatzistergos et al. 2019). The second composite includes measurements of sunspot group area, daily total sunspot area and the photometric sunspot index (PSI) for the period 1874-2019, calculated after cross-calibration of measurements by different observers (Mandal et al. 2020).

Plage and sunspot areas at times when measurements were not available were estimated using the method described in Sec. 3, which makes use of the correlations between the plage and sunspot areas and the solar modulation potential. To this aim, we employ annual estimates of the solar modulation potential derived from the analysis of the ^{14}C (Muscheler et al. 2007) [1] extending from 1000 to 2001 A.D.

The Empirical Mode Decomposition (e.g. Huang et al. 1998) of the solar modulation potential, described in Sec. 4, provides the long term modulation, while the dimensionless weights of the plage and sunspot coverages are obtained by fit with available TSI data, as provided by PMOD composite (Willson 2014) [2].

3. PLAGE AND SUNSPOT COVERAGES RECONSTRUCTION

As mentioned in the previous section, the first step of the proposed methodology consists in the estimate of plage and sunspot areas coverage at times when measurements were not available. Following the approach described in

---

[1] The dataset is available on the NOAA website (https://www.ncdc.noaa.gov/paleo-search/).

[2] available at https://www.pmodwrc.ch/en/research-development/solar-physics/tsi-composite/

Penza et al. (2021), we characterize each cycle through the functional form given in Volobuev (2009)

$$x_k(t) = \left(\frac{t - T0_k}{Ts_k} \right)^2 e^{-\left(\frac{t-T0_k}{Td_k} \right)^2} \qquad \text{for} \quad T0_k < t < T0_k + \tau_k \tag{1}$$

where $T0_k$ is the time that marks the start of cycle k, and Ts_k and Td_k are two free parameters that describe the rising phase and the amplitude of the cycle. For this study we employed the starting times published in (Hathaway et al. 1994; Hathaway 2015). In practice, because cycles with large amplitude are typically characterized by a shorter rising phase (this is known as the Waldemeier effect, Hathaway et al. 1994; Hazra et al. 2015) Ts_k and Td_k are not independent variables. Volobuev (2009) found that these two variables are linearly correlated. We use the functional form in Eq. 1 to fit the sunspot and plage coverage data for all available solar cycles. The scatter plots of the derived Td_k versus Ts_k values are shown in Fig. 1 for both plages and sunspots. The error bars represent the uncertainties returned from the fitting procedure (Bevington & D.K. 2003). Following Volobuev (2009), we perform a linear fit to the data. Many methods have been proposed for performing linear regression when intrinsic scatter is present and both variables are measured with error. Here we used the Bayesian approach described in Kelly (2007) to determine the regression coefficients and their corresponding uncertainties. We find that the dependence of Td_k from Ts_k is described by the following relationships:

$$Td_k^{plage} = (0.10 \pm 0.02)Ts_k^{plage} + (3.14 \pm 0.33) \quad yr$$
$$Td_k^{spot} = (0.02 \pm 0.01)Ts_k^{spot} + (3.14 \pm 0.43) \quad yr. \tag{2}$$

The Pearson correlation coefficients between Ts_k and Td_k are r=0.81 and r=0.70 for plage and sunspot, respectively.
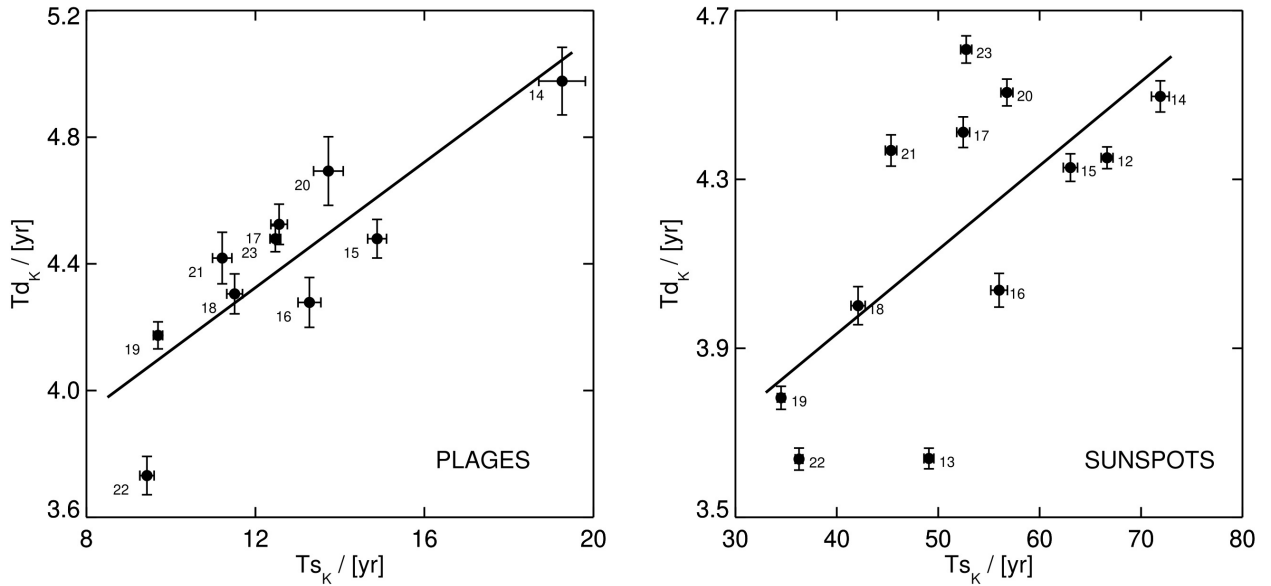

Figure 1. Relationship between the parameters Td_k and Ts_k for plage (left) and sunspot (right) areas. The sunspot data include the additional cycles 12 and 13. The filled circles, with 1-σ error bars, show the data averaged over the individual solar cycle numbers. The regression lines, computed using a Bayesian method (Kelly 2007), are given by Eq. 2.

To estimate the statistical significance of these correlations we performed a t-test and found there is a non-zero correlation between Ts_k and Td_k, at a confidence level greater than 99% for plages and greater than 95% for spots. By inserting these relationships in Eq. 1, we obtain a one-parameter functional form for the shape of the cycles:

$$x_k^{plage}(t) = \left(\frac{t - T0_k}{Ts_k} \right)^2 e^{-\left(\frac{t-T0_k}{0.1Ts_k+3.14} \right)^2} \qquad \text{for} \quad T0_k < t < T0_k + \tau_k$$

$$x_k^{spot}(t) = \left(\frac{t - T0_k}{Ts_k}\right)^2 e^{-\left(\frac{t-T0_k}{0.02Ts_k + 3.14}\right)^2} \qquad \text{for} \quad T0_k < t < T0_k + \tau_k \tag{3}$$

We use the new functional form in Eq. 3 to repeat the fit procedure and to obtain two new dataset of Ts_k values for sunspots and plages. The temporal variation of the area coverages of plage and sunspot is therefore reproduced as summatory on cycle number k of the functional forms x_k. The parametric reconstructions for plage and sunspot area are reported in Fig. 2. The shaded areas in the figure represent the 1-σ confidence level values estimated by taking into account the errors on the fit parameters. This region is more evident in the plage case, while it is practically indistinguishable in the sunspots case. We note that both the reconstructed area coverages well reproduce the observed values. It should also be noted that, as expected, Ts_k^{plage} and Ts_k^{spot} are strongly correlated. The Pearson correlation coefficient is 0.98 and, as shown in Fig. 3, their dependence is well described by the following linear relationship:

$$Ts_k^{spot} = (4.9 \pm 1.4)Ts_k^{plage} - (13.3 \pm 16.4) \quad yr \tag{4}$$

The parameterization described above allows us to characterize each cycle through a single parameter (Ts_k). We
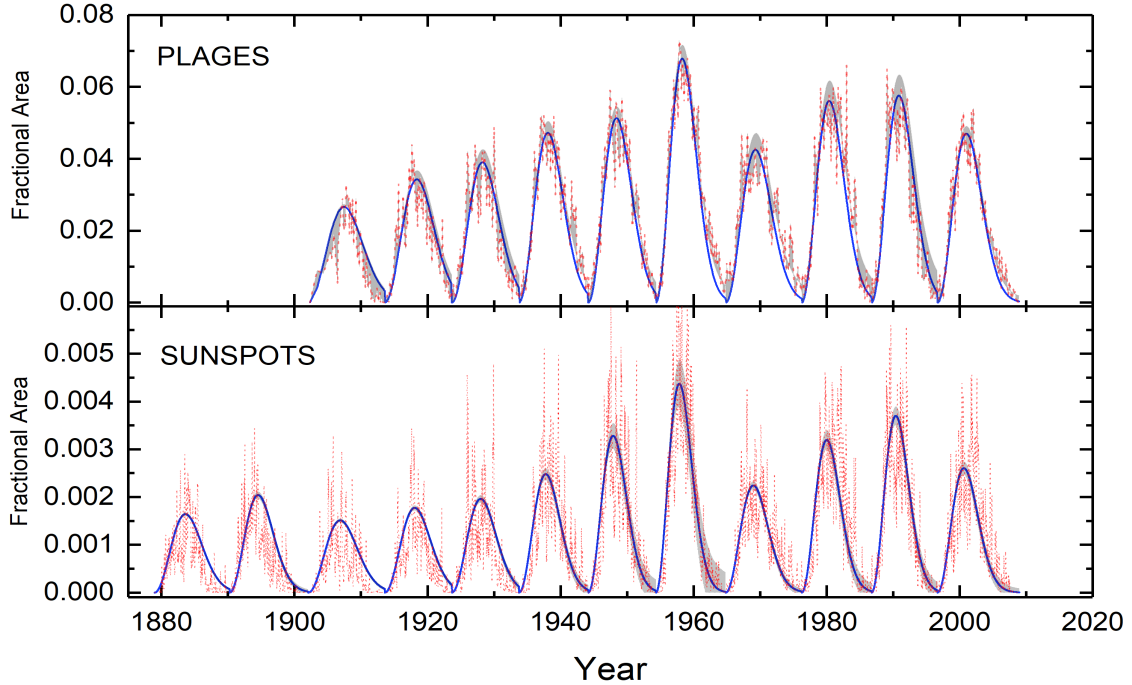
Figure 2. *Upper panel:* Parametric reconstruction of the plage coverage (blue line) with confidence range (gray). The plage composite from the MPI is shown for comparison (red line). *Lower panel:* Parametric reconstruction of the Sunspot coverage (blue line) with confidence range (gray). **The reduction in the confidence range before 1940 is due to the lower SSN which makes it no longer appreciable.** The Sunspot composite from MPI is shown for comparison (red line).

then use the solar modulation potential to reconstruct the shape of each solar cycle for periods when plage and sunspot measurements were not available. In Fig. 4 we show the scatter plot between the plage parameter Ts_k^{plage} and the solar modulation potential $< \Phi >_k$ for each cycle k. Here $< \Phi >_k$ is the averaged-integral value of the solar modulation potential over each cycle. The dependency of the parameter Ts_k^{plage} on the solar modulation potential $< \Phi >_k$ is well described by the following relation:

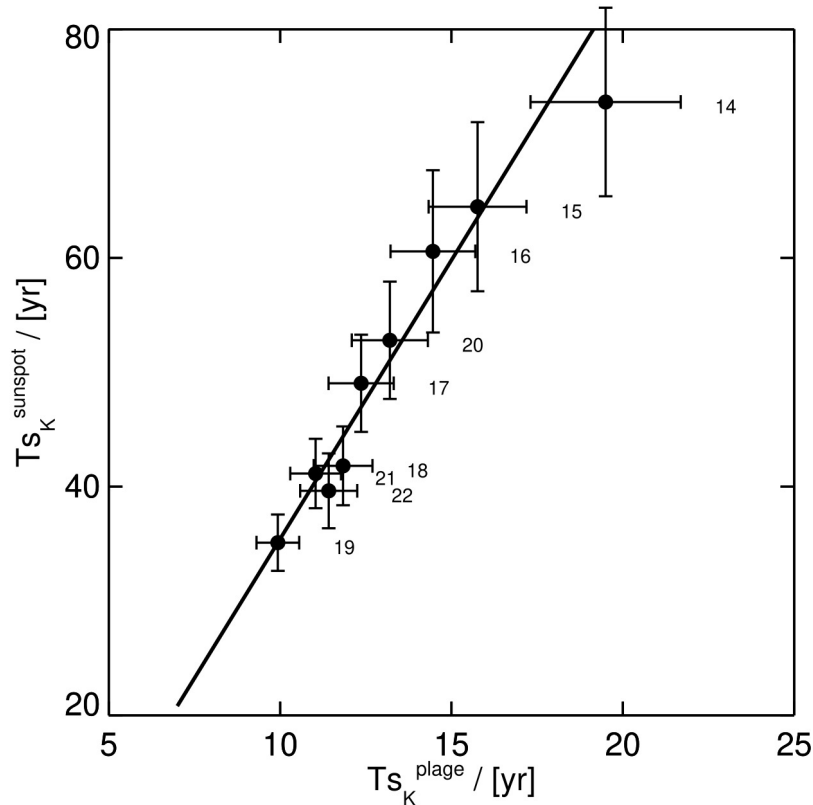$$Ts_k^{plage} = -(0.011 \pm 0.002) < \Phi >_k + (18.5 \pm 1.5) \quad yr \tag{5}$$

Figure 3. Correlation between $Ts_k^{sunspot}$, sunspot parameter, and Ts_k^{plage}, plage parameter. The error bars are 1-σ standard error of the mean for both the sunspot and plage data. The regression line, computed using a Bayesian method (Kelly 2007), is given by Eq.4

.

The Pearson's correlation coefficient is -0.77, at a confidence level greater than 95%.   We use Eq. 5 to reconstruct the plage coverage trend back in time. We decided to consider the Φ data starting from 1513, because before this date the sampling of the solar modulation potential data no longer shows the 11-year cycle modulation due to a much lower temporal sampling from the IntCal04 calibration curve as reported in Muscheler et al. (2007).

In Fig. 5 we plot the composite of the plage coverage, that consists of the reconstructed plage area obtained using Eq. 5 (for the period 1513-1902) and the original observed data (from 1902 to 1996). The reconstruction is shown as a "strip" that takes into account the error propagation of the Ts values in the functional form in Eq. 1. The values of cycle start data $T0_k$ and of cycle duration τ_k, that are not free parameters, are imposed from 1755, i.e. from Cycle 1, by using the data available at SILSO website [3], and Hathaway (2015) while before 1755 by using directly the trend of the solar modulation potential. The values are reported in Table 1.

In order to reconstruct the sunspot area coverage back to 1513 we used the linear relation between Ts_k^{plage} and Ts_k^{spot} described in Eq. 4. The resulting composite of sunspot area coverage is shown in Fig. 6.

4. DECOMPOSITION OF SOLAR MODULATION POTENTIAL Φ

In the introduction of this paper we discussed the joint contribution of the quiet Sun and of photospheric magnetic structures, i.e., sunspots, faculae, network, to the TSI variability. Although we know that the contribution of the quiet Sun's magnetic field is negligible, at least on the scale of ten years of the solar cycle, we cannot exclude that variations of the quiet Sun could play a role in modulating the TSI on longer temporal scales. To estimate the long-term modulation

---

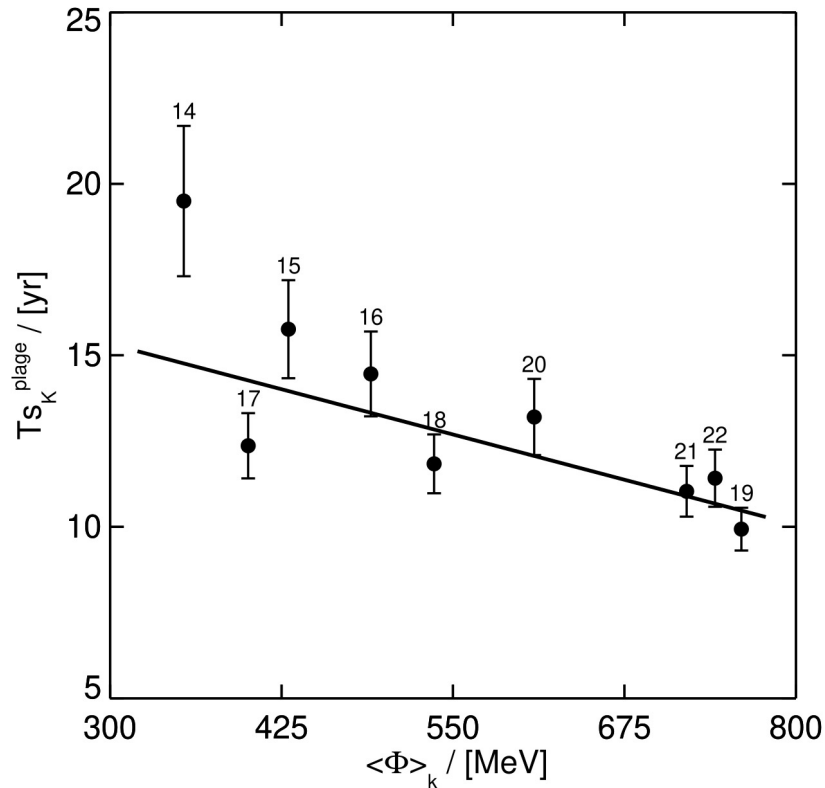[3] The table of minima, maxima and cycle durations are available on SILSO link: https://wwwbis.sidc.be/silso/cyclesmm.

Figure 4.   Dependency of the parameter Ts_k on the k-cycle averaged solar modulation potential $_k$. Individual solar cycle numbers are indicated in the plot, while the error bars are 1-σ standard error of the mean. This relationship is well described by the linear model (solid line) given by Eq. 5. The Pearson's correlation coefficient is -0.77, at a confidence level greater than 95%.

in the TSI and separate the possible contributions to the TSI of the different solar magnetic structures we resort to a decomposition of the temporal modes present in the solar modulation potential, which, as already stated in Sec. 2, we assume to be a proxy of solar surface magnetism. In order to separate the different time-scale components of the solar modulation potential Φ we employ the Empirical Mode Decomposition (EMD) algorithm (Huang et al. 1998). The EMD algorithm is an adaptive and efficient signal decomposition technique, based on the local characteristic time scale of the signal, suitable for nonlinear, chaotic or non-stationary processes. The EMD's intent is to decompose and simplify the original signal into a set of so-called intrinsic mode functions (IMFs) including a monotonic residual. Each IMF, representative of a mode embedded in the data, is calculated *a posteriori* from the signal by a procedure called the sifting process (for more details refer to Huang et al. 1998).

The first step in applying the EMD algorithm to our problem consists in the standardization of the solar potential Φ and of the fractional solar disk coverage by sunspots α_s. The standard score, or Z-score, is calculated as:

$$z = \frac{x - \mu}{\sigma} \tag{6}$$

where z is the dimensionless standardized signal, x is the original signal (i.e., ϕ and α_s), μ and σ the mean and the standard deviation, respectively. Shown in Fig. 7 are the standardized potentials $\hat{\phi}$ and the standardized sunspots coverage area $\hat{\alpha}_s$. To identify and extract the long-term components present in the $\hat{\Phi}$ signal we use the EMD procedure as described in the next section.

4.1.   *Estimate of $\hat{\Phi}$ long-term component based on EMD*
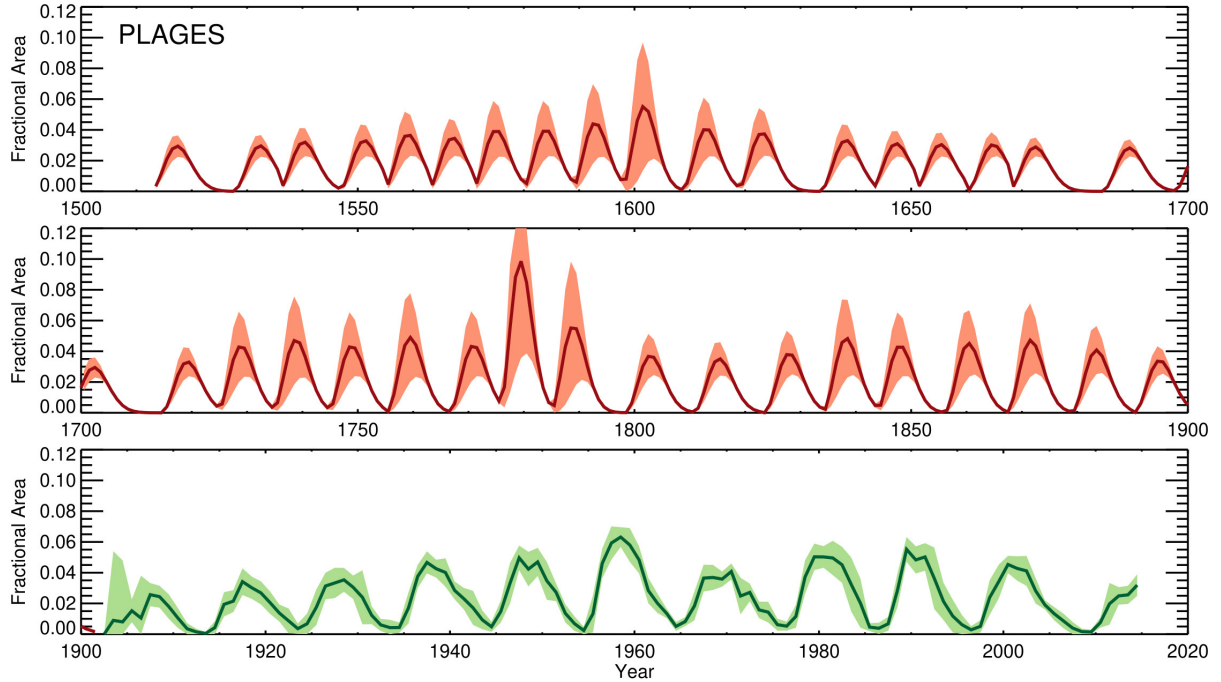
Figure 5. Annual values of the fractional solar disk coverage by plage as a function of time. This composite is derived by merging the values from a reconstructed time series using Eq. 5 (red solid line) and observed data (green solid line). The light-red region indicates the uncertainty range in the reconstructed time series, while the light-green region shows the 5σ confidence interval of the mean annual value.
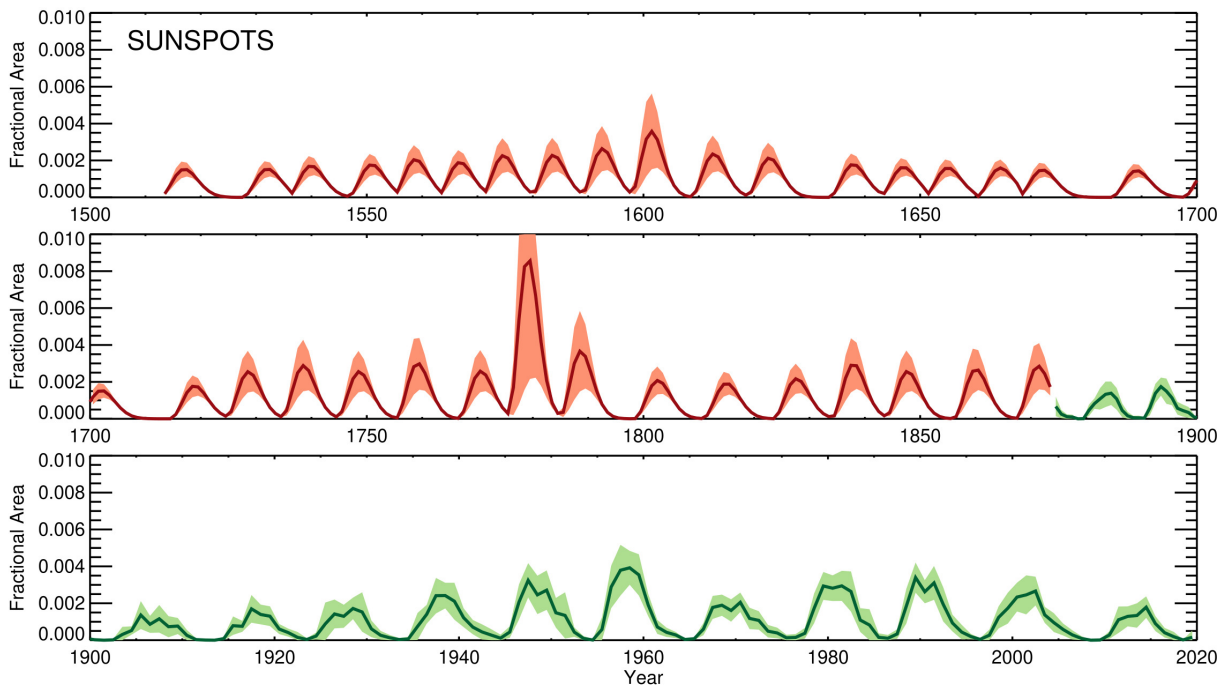

Figure 6. Same as in Fig. 5, but for sunspot data. Here, the light-green region shows the 20σ confidence interval of the mean annual value.

Table 1. Solar Cycle list

Solar Cycle	T0 (yr)	τ (yr)	Solar cycle	T0 (yr)	τ (yr)
-24	1502.5	10.0	-	-	-
-23	1512.5	15.0	1	1755.17	11.33
-22	1527.5	8.0	2	1766.50	9.00
-21	1535.5	11.0	3	1775.50	9.25
-20	1546.5	8.0	4	1784.75	13.58
-19	1554.5	8.0	5	1798.33	12.33
-18	1562.5	8.0	6	1810.67	12.75
-17	1570.5	8.0	7	1823.42	10.50
-16	1579.5	9.0	8	1833.92	9.67
-15	1588.5	9.0	9	1843.583	12.40
-14	1597.5	9.0	10	1855.98	11.27
-13	1608.5	11.0	11	1867.25	11.73
-12	1618.5	10.0	12	1878.98	11.27
-11	1633.5	15.0	13	1890.25	11.83
-10	1642.5	11.0	14	1902.08	11.50
-9	1650.5	8.0	15	1913.58	10.08
-8	1660.5	10.0	16	1923.67	10.08
-7	1667.5	7.0	17	1933.75	10.42
-6	1684.5	17.0	18	1944.17	10.17
-5	1697.5	13.0	19	1954.33	10.50
-4	1714.5	17.0	20	1964.17	11.42
-3	1724.5	10.0	21	1976.25	10.50
-2	1734.5	10.0	22	1986.75	9.92
-1	1744.5	10.67	23	1996.67	12.30

NOTE—In this table are reported the start data (T0) and the duration (τ) of the Solar Cycles

Recall that the goal of EMD algorithm is to decompose a signal into a finite number of basis functions, the IMFs, and a residual $R_n(t)$. A generic signal X(t) is therefore decomposed as:

$$X(t) = \sum_{i}^{n-1} IMF_i(t) + R_n(t) \tag{7}$$

IMFs are oscillatory modes (or components) whose amplitude and period can vary over time, while the residual R(t) is the monotonic trend of the signal. Unlike other signal analysis methods, such as Fourier analysis or wavelets analysis, the basis functions in EMD are not predefined but are empirically calculated from the signal by the algorithm. For these characteristics the EMD method is now widely used in physics and engineering. In solar physics EMD has often been used for its ability to decompose signals that are not simply periodic (e.g. Barnhart & Eichinger 2011; Stangalini et al. 2014; Kolotkov et al. 2016; Lovric et al. 2017; Keys et al. 2018; Vecchio et al. 2019; Bigazzi et al. 2020; Lee 2020). The IMFs of the standardized potential $\hat{\Phi}$ are shown in Fig. 8. The first two components, IMF1 and IMF2, show periodicity associated with the 11-year and 22-year solar magnetic cycles, while the remaining IMFs show longer periods. The residual function shows the monotonic trend of the signal. It is worth remembering that, differently from the sine and cosine components of the Fourier transform, the IMFs represent oscillatory modes whose amplitude and period can vary over time.

At this point it is possible to estimate the secular variation Φ_{LT} by eliminating the common contributions described by the low-order IMFs of $\hat{\Phi}$ and $\hat{\alpha}_s$. Since we want to extract only the long-term solar modulation $\Phi_{LT}(t)$ from $\hat{\Phi}$, we
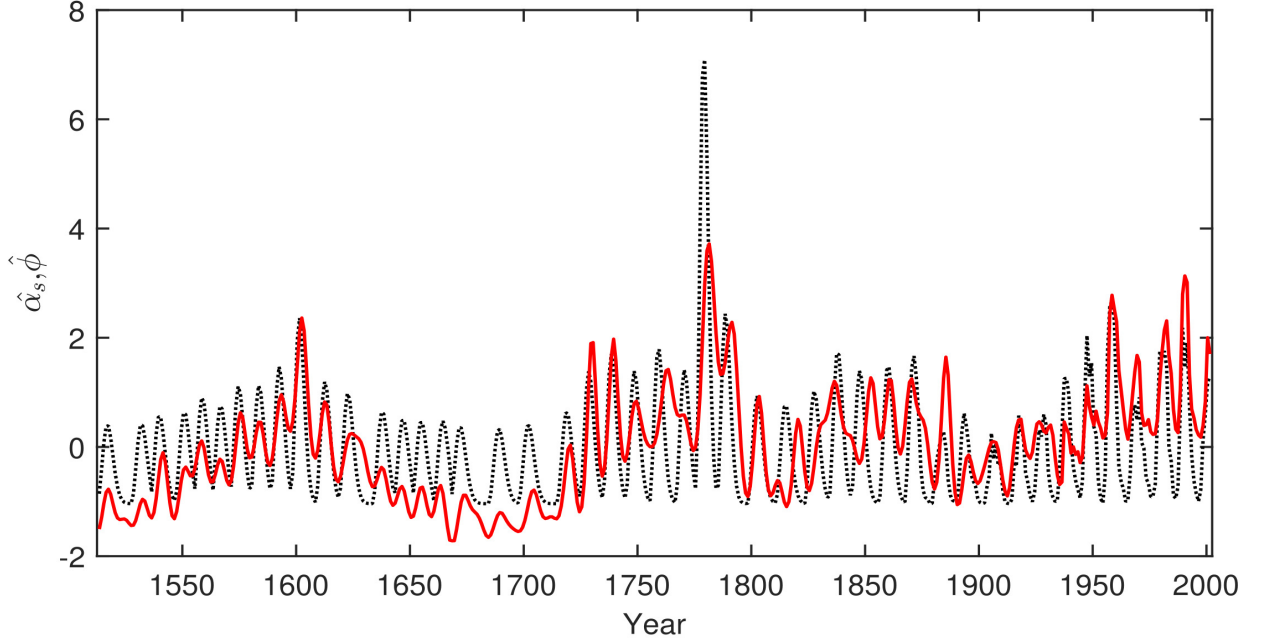
Figure 7. Annual values of the standardized fractional solar disk coverage by sunspots $\hat{\alpha}_s$ (dotted black line) and standardized potential $\hat{\Phi}$ (continuous red line). The sunspots signal has been reconstructed until the 1873, while more recent values are recorded (Mandal et al. 2020).

exclude IMF1 and IMF2 from the reconstruction. Therefore, $\Phi_{LT}(t)$ is obtained from

$$\Phi_{LT}(t) = \sum_{i=3}^{5} C_i \cdot IMF_i(t) + C_R \cdot R(t), \tag{8}$$

where C_i and C_R are parameters which establish the weight of the different normalized IMFs, including the residual $R(t)$, in the final modulation. These parameters are defined so that $\Phi_{LT}(t)$ is the modulation present in $\hat{\Phi}$ but not in α_s. Therefore, we minimize the residuals between $\hat{\Phi}(t)$ and $\hat{\alpha}_s(t) + \Phi_{LT}(t)$ to estimate the free parameters C_i and C_R so that Φ_{LT} represents the secular modulation of the solar modulation potential without the contribution of the modes common with $\hat{\alpha}_s$.

To get the best estimate of the parameters we use a Bayesian approach. More in detail, we use a Monte Carlo Markov Chain (MCMC) algorithm for sampling probability density functions. The Bayes theorem states that:

$$p(\mathbf{C}|\hat{\Phi}(t)) = \frac{p(\hat{\Phi}(t)|\mathbf{C}) \cdot p(\mathbf{C})}{p(\hat{\Phi}(t))} \tag{9}$$

where: *i)* $p(\mathbf{C}|\hat{\Phi}(t))$ is the posterior probability, i.e., the probability of the model of having true parameters $\mathbf{C}$ given the observed data $\hat{\Phi}(t)$, *ii)* $p(\hat{\Phi}(t)|\mathbf{C})$ is the likelihood, i.e., the probability of having $\hat{\Phi}(t)$ given the set of parameters $\mathbf{C}$, and *iii)* $p(\mathbf{C})$ is the prior probability, i.e., the bias on the possible values of the parameters coming from a-priori knowledge. In our analysis, $\mathbf{C}$ are the parameters that we want to estimate (C_3, C_4, C_5, C_R) and $\hat{\Phi}(t)$ the vector of data (i.e., the standardized potential).

Since MCMC algorithms do not depend on the evidence $p(\hat{\Phi}(t))$, by imposing a flat prior probability and a Gaussian likelihood function we have

$$\ln p(\theta|\hat{\mathbf{\Phi}}) = -\frac{1}{2}\sum_{t=1}^{N}(\hat{\Phi}(t) - \Phi_{LT}(t) - \hat{\alpha}_s(t))^2 \tag{10}$$

where t is the discrete time, in years, over which the functions are estimated, and N=489 is equal to the total number of years used (discrete time-domain). The MCMC algorithm used here is the Goodman-Weare (Goodman & Weare
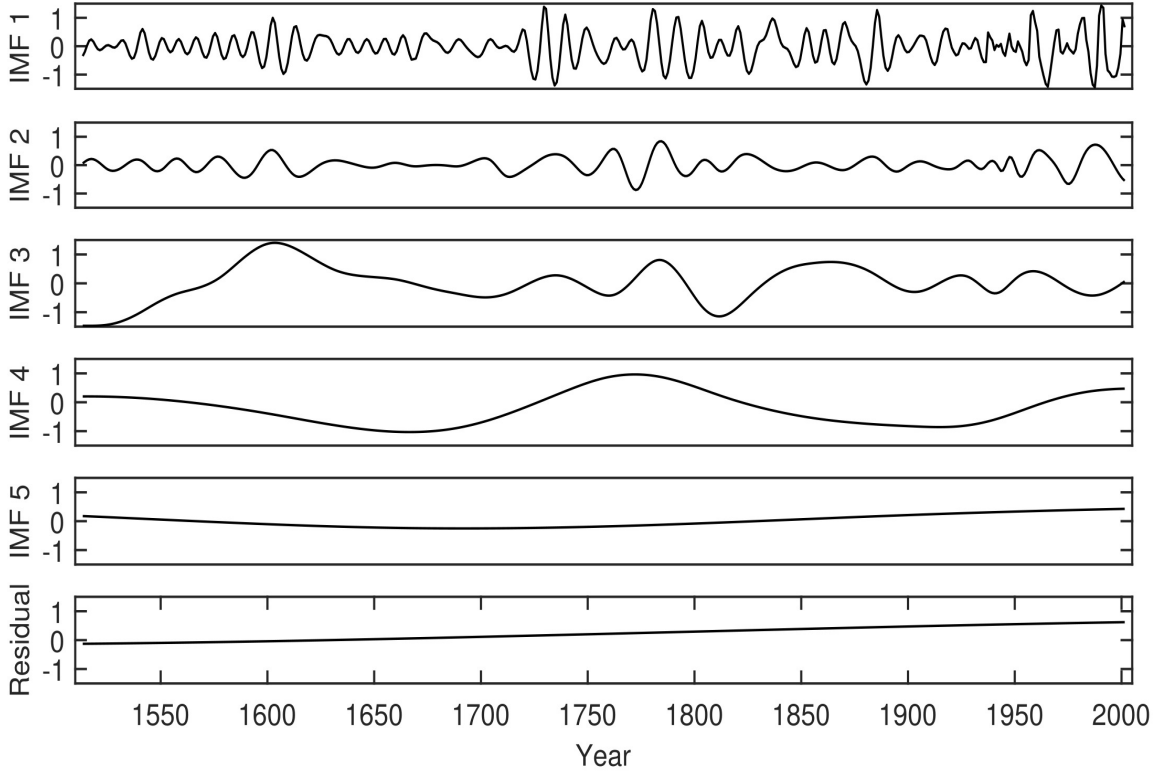
Figure 8. Empirical Mode Decomposition of the standardized potential $\hat{\Phi}$. The IMFs and the residual are shown.IMF1 and IMF2 capture the shortest periods, i.e., periods of approximately 11 years and 22 years, respectively. The residual shows the monotonic trend of the signal. The ordinates have the same scale, so the IMFs can be easily compared.

2010), implemented in Python (Foreman-Mackey et al. 2013). To estimate the most probable values of the different weights C_i and estimate their confidence interval at 1σ we performed a suitable number of tests (i.e., 5000 iterations and 50 chains). The calculated values for the C_i are: $C_3 = 0.33 \pm 0.05$, $C_4 = 0.26 \pm 0.05$, $C_5 = 0.22 \pm 0.05$, and $C_R = 0.15 \pm 0.04$, respectively.

5. TSI RECONSTRUCTION

Like other methods presented in the literature (see Sec. 1), our TSI reconstruction is based on the assumption that irradiance is modulated by solar surface magnetism. Specifically, we assume that the solar irradiance F at time t is given by:

$$F(t) = \sum_j \alpha_j(t)F_j, \tag{11}$$

where F_j is the contribution to the TSI from the j-feature (quiet, network, facula, and sunspot) and $\alpha(t)_j$ is the respective coverage. We use the reconstructed plage coverage area as proxy of the facular coverage $\alpha_f(t)$ (see Gray et al. (2010)). We further assume that only the surface coverages change with the time, while the average contrasts are time-independent. We rewrite the Eq. 11 by expliciting the network, facular and sunspot contributions:

$$F(t) = F_q(1 - \alpha_n(t) - \alpha_f(t) - \alpha_s(t)) + \alpha_n(t)F_n + \alpha_f(t)F_f + \alpha_s(t)F_s \tag{12}$$

where the subscripts n, f and s indicate network, facular and sunspot component, respectively. We adopt a linear correlation between α_n and α_f (e.g. Criscuoli et al. 2018; Devil et al. 2021):

$$\alpha_n = (A_n + B_n\alpha_f(t)). \tag{13}$$

So that

$$F(t) = F_q + (F_n - F_q)(A_n + B_n\alpha_f(t)) + (F_f - F_q)\alpha_f(t) + (F_s - F_q)\alpha_s(t). \tag{14}$$

The equation can be simplified if we rewrite it as a relative variation with respect to the radiative flux of the Quiet Sun:

$$\Delta F(t) = \frac{F(t) - F_q}{F_q} = A_n \frac{F_n - F_q}{F_q} + \alpha_f(t) B_n \frac{F_n - F_q}{F_q} + \alpha_f(t) \frac{F_f - F_q}{F_q} + \alpha_s(t) \frac{F_s - F_q}{F_q} \tag{15}$$

$$\Delta F(t) = A_n \delta_n + \alpha_f(t)(B_n \delta_n + \delta_f) + \alpha_s(t)\delta_s = C_n + \alpha_f(t)\delta_{fn} + \alpha_s(t)\delta_s \tag{16}$$

where C_n is a constant and represent the product between the network contrast and the network coverage when the facular coverage is zero, δ_{fn} is a linear combination of network and facular relative contrast, while δ_s is the sunspot relative contrast. The values of C_n, δ_{fn} and δ_s are estimate by best fitting Eq. 16 with measurements of TSI variability [4] along Solar Cycle 22 and 23. We fit the two cycles separately in order to consider the long-term component negligible, and for each cycle we use the corresponding measured α_s and α_f. As values for the TSI reconstruction we take the average of the two set of C_n, δ_{fn} and δ_s estimated from the two fits:
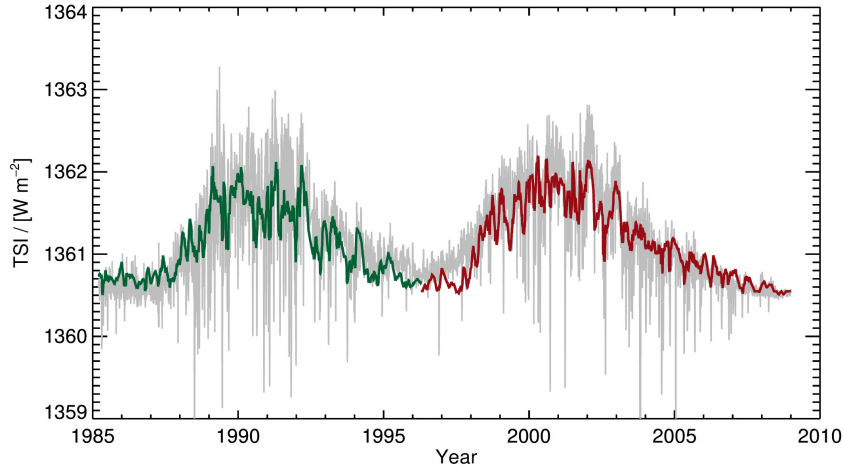
Figure 9. Comparison between the TSI PMOD-composite (in grey) and the reconstructed TSI time series for solar cycles 22 (green) and 23 (red). The TSI reconstruction was computed independently for cycle 22 and 23 (see text).

$$C_n = \frac{C_n^{(22)} + C_n^{(23)}}{2} = \frac{(1.28 \cdot 10^{-3} \pm 5 \cdot 10^{-5}) + (1.34 \cdot 10^{-3} \pm 7 \cdot 10^{-5})}{2} = 1.31 \cdot 10^{-3} \pm 6 \cdot 10^{-5}$$

$$\delta_{fn} = \frac{\delta_{fn}^{(22)} + \delta_{fn}^{(23)}}{2} = \frac{(0.029 \pm 0.005) + (0.025 \pm 0.003)}{2} = 0.027 \pm 0.004$$

$$\delta_s = \frac{\delta_s^{(22)} + \delta_s^{(23)}}{2} = \frac{(-0.16 \pm 0.05) + (-0.18 \pm 0.07)}{2} = -0.17 \pm 0.06$$

$$\tag{17}$$

The measured and reconstructed TSI for Cycle 22 and Cycle 23 are shown in Fig. 9. The TSI absolute values are obtained by setting the F_q value to the TSI value measured at the 1986 minimum. The choice of this minimum as the baseline for normalization has no substantial effect in the final reconstruction, as the fluxes of measured minima differ no more than $0.2 W m^{-2}$.

Although we have imposed no constraints on the model, we note that the values of the fitted parameters are not significantly different from others reported in the literature. For example, our result of C_n is consistent with results of Foukal et al. (1991), that provide a value of the network contrast weighted by corresponding fractional area at the solar minimum of about $1.08 \cdot 10^{-3}$. Similarly, the value of δ_{fn} represents a sensible mixed facular and network bolometric

---

[4] specifically we use the composite available at https://www.pmodwrc.ch/en/research-development/solar-physics/tsi-composite/

contrast (e.g. Foukal et al. 2004). The sunspot bolometric contrast, however, results about 50% less intense than the values reported in the literature (e.g. Chapman et al. 1994; Walton et al. 2003).

In order to reproduce the TSI over temporal scales longer than the decadal one, we modulate the network component (C_n), present even in the absence of other magnetic structures. In this way, we attribute to this parameter all the effects of the open or "hidden" magnetic field and we rewrite the Eq. 16 as

$$\Delta F(t) = C_n mod_\Phi(t) + \alpha_f(t)\delta_{fn} + \alpha_s(t)\delta_s \qquad (18)$$

To derive the modulation function $mod(\Phi)$, we consider the residual composition of IMFs of Φ as explained in Section 5. The modulation function $mod(\Phi)$ is the long-term component of the solar modulation potential Φ_{LT} described in Sec. 4, properly normalized. We impose a normalization parameter as following:

$$mod_\Phi(t) = (\Phi_{LT}(t) + 1)N_{ref} \qquad (19)$$

and determine the parameter N_{ref} by best fit optimizing the comparison with the entire PMOD TSI composite of TSI and obtaining the value $N_{ref} = 0.38 \pm 0.02$.

Eventually, we can reconstruct the behavior of the TSI in the period (1513-2001). The estimated TSI, reconstructed using the approach proposed in this work, is shown in Fig. 10, together with the TSI proposed by Wu et al. (2018), SATIRE, Egorova et al. (2018), CHRONOS, and Coddington et al. (2019), NRL-TSIv2.

6. DISCUSSION AND CONCLUSIONS

In this work we present a reconstruction of the total solar irradiance variability from the pre-industrial era to the present. Our approach uses modern TSI measurements to estimate the contribution of sunspots and faculae in terms of area coverages and bolometric contrast, and the solar modulation potential to take into account for the long-term (longer than 22 years) variation of a quiet component. It's worth noting that our estimates of area coverage are in agreement with the values derived directly from the observations of sunspots and faculae (see Fig. 5 and Fig. 6). Moreover, our estimated values for the bolometric contrast are in agreement with values reported in literature (for a complete discussion see Sec. 5).

Regarding TSI, our reconstruction produces a variation from the Maunder minimum to the present of approximately 2.5 Wm^{-2}. This value is in between those obtained with models that do not take into account secular variations of a quiet component, such as SATIRE (Wu et al. 2018) and NRL-TSI (Coddington et al. 2016) (0.28 and 0.55 Wm^{-2}, respectively), and several Wm^{-2} obtained by models that postulate a long term variation of the quiet Sun, as Egorova et al. (2018) or Shapiro et al. (2011b), the latter not shown in Fig2.5 Wm^{-2}. 10.

Our reconstruction shows a reduced secular modulation compared to estimates by Egorova et al. (2018) and Shapiro et al. (2011b). This is due to two important differences with respect to their approach: *i)* we modulated a (quiet) network component, whose radiative emission is empirically derived from observations; *ii)* we took into account only of secular variations of the modulation potential, by empirically decomposing the signal into six components and discarding variations ascribable to the Hale magnetic solar cycle (11-years and 22-years components). The long term modulation has been obtained as the weighted sum of the considered components. The weights have been assigned so that the long-term trend will be present in the modulation of the solar potential but not in the sunspots coverage areas series.

Both of these aspects affect the amplitude and shape of the modelled variability. Egorova et al. (2018) noted the the amplitude of the variability is strongly affected by the choice of the atmosphere model modulated by the solar modulation potential. The fact that we modulated a bright quiet network component most likely is one of the major factors producing lower TSI variability from the Maunder minimum to modern times than Shapiro et al. (2011a) and Egorova et al. (2018). The fact that we employed higher order Empirical Modes of the solar modulation potential instead of a 22-years smoothed mean most likely explain the differences found in the shape and phase of the TSI variability. In particular, we note that during the Maunder minimum our reconstructed TSI presents a slow decline and only a slightly faster increase starting around 1680, while reconstructions by Shapiro et al. (2011a) and Egorova et al. (2018) present a steeper decrease, reach a minimum around 1700, and rapidly increase. Similar differences are found for the Dalton minimum and the 1900 minimum.

We note that our reconstruction for the period before 1751 is closely linked to the trend in the solar modulation potential, which produces an inevitable modulation during the Maunder minimum. There are indications in literature
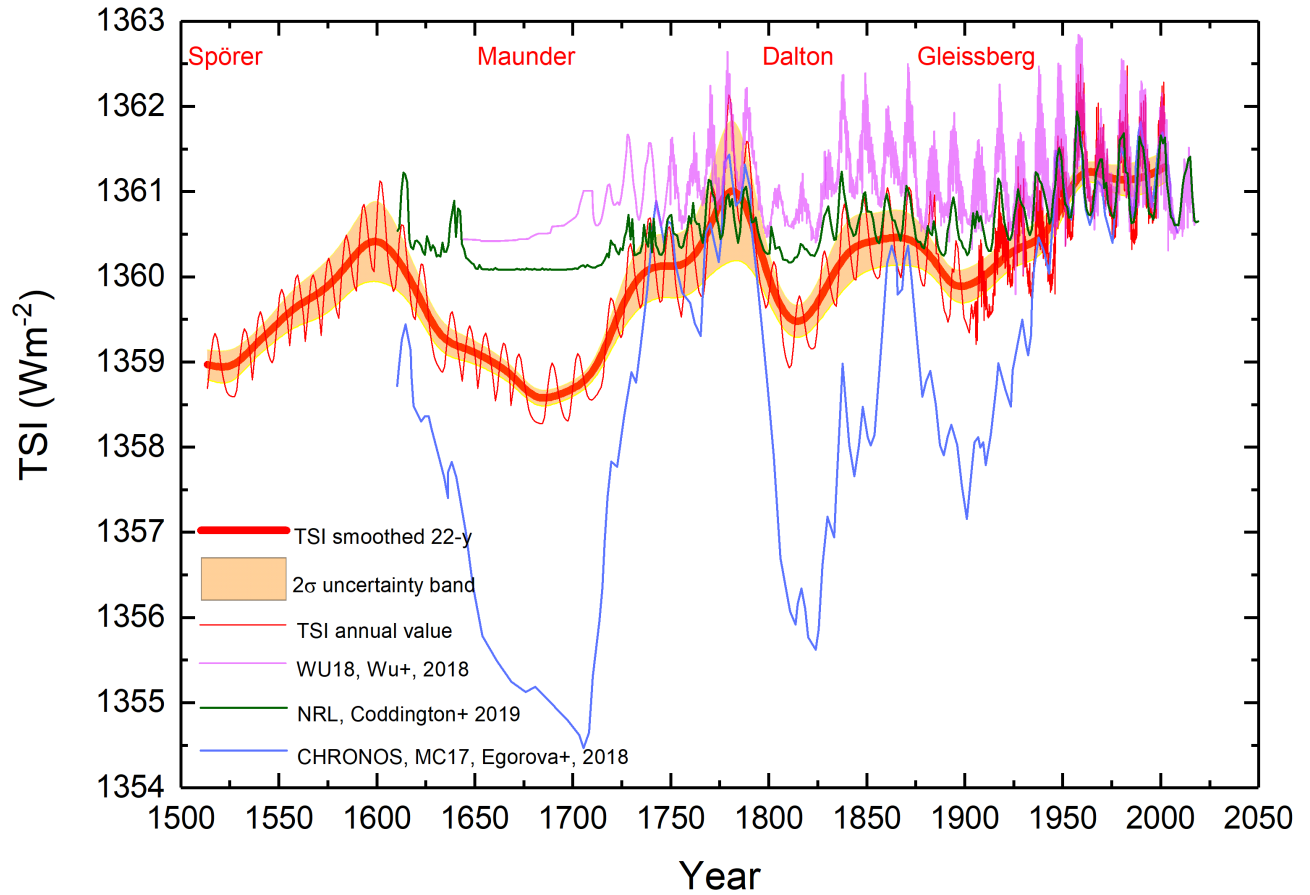
Figure 10. Four reconstructions of TSI are reported, obtained with different methods for comparison purposes only. Our TSI reconstruction is shown as a continuum red line; the red bold line is the TSI smoothed over a period of 22 yr with a $2 - \sigma$ uncertainty orange stripe. The NRL TSI data Climate Data Record (green line) from Coddington et al. (2019). TSI values from Wu et al. (2018) (magenta). CHRONOS, MC17 TSI values from Egorova et al. (2018) (blue). The names refer to the grand minima that occurred in the analyzed period, i.e., Spörer, Munder, Dalton and Gleissberg.

of a residual magnetic activity during that period (e.g. Zolotova & Ponyavin 2015; Kopp et al. 2016b; Jungclaus et al. 2017), smaller than it is reported here. Our result is related to assumption of the constancy of the correlations in Eq. 5 back in time. However, that does not affect the final result of the average trend of the TSI shown in bold red line in Fig.10.

Recently, limits to the variability of the TSI from the Maunder minimum to the present were estimated by the works of Lockwood & Ball (2020) and Yeo et al. (2020). Lockwood & Ball (2020) assumed that the difference between current models and composite measurements provide an estimate of the quiet Sun secular component. By correlating these differences with the solar modulation potential, they estimated that the TSI changes between the Maunder minimum and the present must range between -0.95 and 1.98 Wm^{-2}, the negative value indicating that the TSI decreased from the Maunder minimum to the present. Yeo et al. (2020) suggested instead that the quiet possible state for the solar photosphere can be represented by local-dynamo three dimensional magneto-hydrodynamic simulations, and estimated an upper limit increase from the Maunder minimum to the present of about 2 Wm^{-2}. Our estimate of about 2.5 Wm^{-2} is consistent with these values.

It is noteworthy that the TSI exhibits particularly high values during solar cycle 3 (Fig. 10), although compatible

within the error with other TSI reconstructions. As discussed in section 5, the value of the TSI depends primarily on the disk coverage by faculae (plages) and sunspots, and this coverage was significantly high during that particular cycle (see Fig.5 and Fig.6). The analysis of Fig.7 suggests that this is due to the trend in the solar modulation potential Φ, which remained at high levels during cycle 3 and 4. This behavior in Φ is a consequence of the narrow and deep minimum in ^{14}C radiocarbon measurements observed around the maxima of these two cycles. This deep ^{14}C minimum is present in the dataset used in this work, but it is also reported in other datasets (e.g. Brehm et al. 2021).

In conclusion, the main findings of our work can be summarized in the following five points:

1. we reconstruct the area coverage of faculae (plages) and sunspots from 1513 to 2001 using their cycle-by-cycle observed correlation with the solar modulation potential Φ over the last century.

2. we estimate the long-term modulation in the TSI and separate the contributions to the TSI of the different solar magnetic structures through the Empirical Mode Decomposition of the solar modulation potential Φ;

3. our Total Solar Irradiance reconstructed time series from 1513 to 2001 shows a behavior that is somewhat intermediate between other reconstructions proposed in the literature;

4. we estimate that the change in TSI levels between the Maunder minimum and the present epoch is approximately $2.5 W m^{-2}$;

5. we estimate a growth in the TSI value of about $1.5 W m^{-2}$ during the first half of last century. After the 1950s, this value has remained substantially constant (on average) until the beginning of this century.

REFERENCES

Ball, W. T., Krivova, N. A., Unruh, Y. C., Haigh, J. D., & Solanki, S. K. 2014, Journal of Atmospheric Sciences, 71, 4086, doi: 10.1175/JAS-D-13-0241.1

Ball, W. T., Unruh, Y. C., Krivova, N. A., et al. 2012, A&A, 541, A27, doi: 10.1051/0004-6361/201118702

Barnhart, B. L., & Eichinger, W. E. 2011, Journal of Atmospheric and Solar-Terrestrial Physics, 73, 1771, doi: 10.1016/j.jastp.2011.04.012

Berrilli, F., Criscuoli, S., Penza, V., & Lovric, M. 2020, SoPh, 295, 38, doi: 10.1007/s11207-020-01603-5

Berrilli, F., Ermolli, I., Florio, A., & Pietropaolo, E. 1999, A&A, 344, 965

Bertello, L., Pevtsov, A. A., & Ulrich, R. K. 2020, ApJ, 897, 181, doi: 10.3847/1538-4357/ab9746

Bevington, P., & D.K., R. 2003

Bigazzi, A., Cauli, C., & Berrilli, F. 2020, Annales Geophysicae, 38, 789, doi: 10.5194/angeo-38-789-2020

Bolduc, C., Charbonneau, P., Dumoulin, V., Bourqui, M. S., & Crouch, A. D. 2012, SoPh, 279, 383, doi: 10.1007/s11207-012-0019-4

Bordi, I., Berrilli, F., & Pietropaolo, E. 2015, Annales Geophysicae, 33, 267, doi: 10.5194/angeo-33-267-2015

Brehm, N., Bayliss, A., Christl, M., et al. 2021, Nature Geoscience, 14, 10, doi: 10.1038/s41561-020-00674-0

Chapman, G. A., Cookson, A. M., & Dobias, J. J. 1994, ApJ, 423, 403, doi: 10.1086/174578

Chatzistergos, T., Ermolli, I., Krivova, N. A., & K., S. S. 2019, A&A, 625, 22, doi: 10.1051/0004-6361/201834402

Coddington, O., Lean, J. L., Pilewskie, P., Snow, M., &
    Lindholm, D. 2016, Bulletin of the American
    Meteorological Society, 97, 1265,
    doi: 10.1175/BAMS-D-14-00265.1

Coddington, O., Lean, J. L., Pilewskie, P., et al. 2019,
    Earth and Space Science, 6, 2525,
    doi: 10.1029/2019EA000693

Criscuoli, S. 2019, ApJ, 872, 52,
    doi: 10.3847/1538-4357/aaf6b7

Criscuoli, S., & Foukal, P. 2017, ApJ, 835, 99,
    doi: 10.3847/1538-4357/835/1/99

Criscuoli, S., Penza, V., Lovric, M., & Berrilli, F. 2018,
    ApJ, 865, 22, doi: 10.3847/1538-4357/aad809

Devil, P., Singh, J., Chandra, R., Priyal, M., & Josh, R.
    2021, SoPh, 296, 49, doi: 10.1007/s11207-021-01798-1

Dudok de Wit, T., & Kopp, G. 2020, in IAU General
    Assembly, 336–338, doi: 10.1017/S174392131900454X

Dudok de Wit, T., Kopp, G., Fröhlich, C., & Schöll, M.
    2017, Geophys. Res. Lett., 44, 1196,
    doi: 10.1002/2016GL071866

Egorova, T., Schmutz, W., Rozanov, E., et al. 2018, A&A,
    615, A85, doi: 10.1051/0004-6361/201731199

Ermolli, I., Berrilli, F., & Florio, A. 2003, A&A, 412, 857,
    doi: 10.1051/0004-6361:20031479

Ermolli, I., Criscuoli, S., & Giorgi, F. 2011, Contributions
    of the Astronomical Observatory Skalnate Pleso, 41, 73

Fabbian, D., Simoniello, R., Collet, R., et al. 2017,
    Astronomische Nachrichten, 338, 753,
    doi: 10.1002/asna.201713403

Faurobert, M. 2019, Chapter 8 - Solar and Stellar
    Variability, ed. O. Engvold, J.-C. Vial, & A. Skumanich,
    267–299, doi: 10.1016/B978-0-12-814334-6.00010-8

Faurobert, M., Criscuoli, S., Carbillet, M., & Contursi, G.
    2020, A&A, 642, A186,
    doi: 10.1051/0004-6361/202037736

Fontenla, J., White, O. R., Fox, P. A., Avrett, E. H., &
    Kurucz, R. L. 1999, ApJ, 518, 480, doi: 10.1086/307258

Fontenla, J. M., Codrescu, M., Fedrizzi, M., et al. 2017,
    ApJ, 834, 54, doi: 10.3847/1538-4357/834/1/54

Fontenla, J. M., Harder, J., Livingston, W., Snow, M., &
    Woods, T. 2011, Journal of Geophysical Research
    (Atmospheres), 116, D20108, doi: 10.1029/2011JD016032

Fontenla, J. M., Stancil, P. C., & Landi, E. 2015, ApJ, 809,
    157, doi: 10.1088/0004-637X/809/2/157

Foreman-Mackey, D., Hogg, D. W., Lang, D., & Goodman,
    J. 2013, PASP, 125, 306, doi: 10.1086/670067

Foukal, P., Bernasconi, P., Eaton, H., & Rust, D. 2004,
    ApJL, 611, L57, doi: 10.1086/186249

Foukal, P., Harvey, K., & Hill, F. 1991, ApJL, 383, L89,
    doi: 10.1086/186249

Foukal, P., Ortiz, A., & Schnerr, R. 2011, ApJL, 733, L38,
    doi: 10.1088/2041-8205/733/2/L38

Fröhlich, C., & Lean, J. 2004, A&A Rv, 12, 273,
    doi: 10.1007/s00159-004-0024-1

Galuzzo, D., Cagnazzo, C., Berrilli, F., Fierli, F., &
    Giovannelli, L. 2021, ApJ, 909, 191,
    doi: 10.3847/1538-4357/abdeb4

Goodman, J., & Weare, J. 2010, Communications in
    Applied Mathematics and Computational Science, 5, 65,
    doi: 10.2140/camcos.2010.5.65

Gray, L. J., Beer, J., Geller, M., et al. 2010, Reviews of
    Geophysics, 48, RG4001, doi: 10.1029/2009RG000282

Haberreiter, M. 2011, SoPh, 274, 473,
    doi: 10.1007/s11207-011-9767-9

Haberreiter, M., Delouille, V., Mampaey, B., et al. 2014,
    Journal of Space Weather and Space Climate, 4, A30,
    doi: 10.1051/swsc/2014027

Haigh, J. D., Winning, A. R., Toumi, R., & Harder, J. W.
    2010, Nature, 467, 696, doi: 10.1038/nature09426

Hathaway, D. 2015, Living Reviews in Solar Physics, 12,
    87, doi: 1007/lrsp-2015-4

Hathaway, D., Hathaway, D., & Reichmann, J. 1994, SoPh,
    151, 177, doi: 10.1007/BF00654090

Hazra, G., KArak, B., KArak, B.B.and Banerjee, D., &
    A.R., C. 2015, SoPh, 290, 1851–1870,
    doi: 10.1007/s11207-015-0718-8

Huang, N. E., Shen, Z., Long, S. R., et al. 1998,
    Proceedings of the Royal Society of London Series A,
    454, 903, doi: 10.1098/rspa.1998.0193

Hudson, H. S. 1988, ARA&A, 26, 473,
    doi: 10.1146/annurev.aa.26.090188.002353

Häder, D.-P., Helbling, E. W., Williamson, C. E., &
    Worrest, R. C. 2011, Photochem. Photobiol. Sci., 10, 242,
    doi: 10.1039/C0PP90036B

Ineson, S., Maycock, A. C., Gray, L. J., et al. 2015, Nature
    Communications, 6, 7535, doi: 10.1038/ncomms8535

Jungclaus, J. H., Bard, E., Baroni, M., et al. 2017,
    Geoscientific Model Development, 10, 4005,
    doi: 10.5194/gmd-10-4005-2017

Kelly, B. C. 2007, ApJ, 665, 1489, doi: 10.1086/519947

Keys, P. H., Morton, R. J., Jess, D. B., et al. 2018, ApJ,
    857, 28, doi: 10.3847/1538-4357/aab432

Kolotkov, D. Y., Anfinogentov, S. A., & Nakariakov, V. M.
    2016, A&A, 592, A153,
    doi: 10.1051/0004-6361/201628306

Kopp, G. 2014, Journal of Space Weather and Space
    Climate, 4, A14, doi: 10.1051/swsc/2014012

Kopp, G., Krivova, N., Wu, C. J., & Lean, J. 2016a, SoPh,
    291, 2951, doi: 10.1007/s11207-016-0853-x

—. 2016b, SoPh, 291, 2951, doi: 10.1007/s11207-016-0853-x

Kopp, G., & Shapiro, A. 2021, arXiv e-prints,
arXiv:2102.06913. https://arxiv.org/abs/2102.06913

Kren, A. C., Pilewskie, P., & Coddington, O. 2017, Journal
of Space Weather and Space Climate, 7, A10,
doi: 10.1051/swsc/2017007

Krivova, N. A., Balmaceda, L., & Solanki, S. K. 2007,
A&A, 467, 335, doi: 10.1051/0004-6361:20066725

Kutiev, I., Tsagouri, I., Perrone, L., et al. 2013, Journal of
Space Weather and Space Climate, 3, A06,
doi: 10.1051/swsc/2013028

Lean, J. 2017, Oxford Research Encyclopedia,
doi: 10.1093/acrefore/9780190228620.013.9

Lean, J. L. 2018, Earth and Space Science, 5, 133,
doi: 10.1002/2017EA000357

Lean, J. L., Coddington, O., Marchenko, S. V., et al. 2020,
Earth and Space Science, 7, 00645,
doi: 10.1029/2019EA000645

Lee, T. 2020, SoPh, 295, 82,
doi: 10.1007/s11207-020-01653-9

Linsky, J. 2019, Host Stars and their Effects on Exoplanet
Atmospheres, Vol. 955, doi: 10.1007/978-3-030-11452-7

Lockwood, M., & Ball, W. T. 2020, Proc. R. Soc. A., 476,
doi: 10.1098/rspa.2020.0077

Lockwood, M., Harrison, R. G., Woollings, T., & Solanki,
S. K. 2010, Environmental Research Letters, 5, 024001,
doi: 10.1088/1748-9326/5/2/024001

Lovric, M., Tosone, F., Pietropaolo, E., et al. 2017, Journal
of Space Weather and Space Climate, 7, A6,
doi: 10.1051/swsc/2017001

Mandal, S., Krivova, N. A., Solanki, S. K., Sinha, N., &
Banerjee, D. 2020, A&A, 640, A78,
doi: 10.1051/0004-6361/202037547

Martucci, M., Munini, R., Boezio, M., et al. 2018, ApJL,
854, L2, doi: 10.3847/2041-8213/aaa9b2

Matthes, K., Funke, B., Andersson, M. E., et al. 2017,
Geoscientific Model Development, 10, 2247,
doi: 10.5194/gmd-10-2247-2017

Muscheler, R., Joos, F., Beer, J., et al. 2007, Quaternary
Science Reviews, 26, 82,
doi: 10.1016/j.quascirev.2006.07.012

Myers, D. D. 2017, Solar Radiation: Practical Modeling for
Renewable Energy Applications, doi: 10.1201/b13898

Pagaran, J., Weber, M., & Burrows, J. 2009, ApJ, 700,
1884, doi: 10.1088/0004-637X/700/2/1884

Penza, V., Berrilli, F., L., B., Cantoresi, M., & Criscuoli, S.
2021, ApJL, 922, L12, doi: 10.3847/2041-8213/ac3663

Penza, V., Caccin, B., Ermolli, I., Centrone, M., & Gomez,
M. T. 2003, in ESA Special Publication, Vol. 535, Solar
Variability as an Input to the Earth's Environment, ed.
A. Wilson, 299–302

Petrie, G., Criscuoli, S., & Bertello, L. 2021, in Solar
Physics and Solar Wind, ed. N. E. Raouafi &
A. Vourlidas, Vol. 1, 83, doi: 10.1002/9781119815600.ch3

Rast, M. P., Bello González, N., Bellot Rubio, L., et al.
2021, SoPh, 296, 70, doi: 10.1007/s11207-021-01789-2

Rempel, M. 2020, ApJ, 894, 140,
doi: 10.3847/1538-4357/ab8633

Rimmele, T. R., Warner, M., Keil, S. L., et al. 2020, SoPh,
295, 172, doi: 10.1007/s11207-020-01736-7

Rodriguez, F., Ronchini, L. R., Di Rollo, S., et al. 2019,
Nuovo Cimento C Geophysics Space Physics C, 42, 45,
doi: 10.1393/ncc/i2019-19045-6

Schmutz, W. K. 2021, Journal of Space Weather and Space
Climate, 11, 40, doi: 10.1051/swsc/2021016

Schnerr, R. S., & Spruit, H. C. 2011, A&A, 532, A136,
doi: 10.1051/0004-6361/201015976

Schrijver, C. J., Livingston, W. C., Woods, T. N., &
Mewaldt, R. A. 2011, Geophys. Res. Lett., 38, L06701,
doi: 10.1029/2011GL046658

Shapiro, A. I., Fluri, D. M., Berdyugina, S. V., Bianda, M.,
& Ramelli, R. 2011a, A&A, 529, A139,
doi: 10.1051/0004-6361/200811299

Shapiro, A. I., Schmutz, W., Rozanov, E., et al. 2011b,
A&A, 529, A67, doi: 10.1051/0004-6361/201016173

Shindell, D. T., Schmidt, G. A., Mann, M. E., Rind, D., &
Waple, A. 2001, Science, 294, 2149,
doi: 10.1126/science.1064363

Stangalini, M., Consolini, G., Berrilli, F., De Michelis, P., &
Tozzi, R. 2014, A&A, 569, A102,
doi: 10.1051/0004-6361/201424221

Steinhilber, F., Beer, J., & Fröhlich, C. 2009,
Geophys. Res. Lett., 36, L19704,
doi: 10.1029/2009GL040142

Tapping, K. F., Boteler, D., Charbonneau, P., et al. 2007,
SoPh, 246, 309, doi: 10.1007/s11207-007-9047-x

Usoskin, I. G. 2017, Living Reviews in Solar Physics, 14, 3,
doi: 10.1007/s41116-017-0006-9

Vecchio, A., Lepreti, F., Laurenza, M., Carbone, V., &
Alberti, T. 2019, Nuovo Cimento C Geophysics Space
Physics C, 42, 15, doi: 10.1393/ncc/i2019-19015-0

Volobuev, D. 2009, SoPh, 258, 319,
doi: 110.1007/s11207-009-9429-3

Walton, S. R., Preminger, D. G., & Chapman, G. 2003,
SoPh, 203, 301W, doi: 10.1023/A:1023986901169

Wang, Y. M., Lean, J. L., & Sheeley, N. R., J. 2005, ApJ,
625, 522, doi: 10.1086/429689

Wenzler, T., Solanki, S., Krivova, N., & Fröhlich, C. 2006,
A&A, 460, 583, doi: 10.1051/0004-6361:20065752

Willson, R. C. 2014, Astrophysics and Space Science, 352,
341, doi: 10.1007/s10509-014-1961-4

Wilson, O. C. 1978, ApJ, 226, 379, doi: 10.1086/156618

Woodard, M., & Hudson, H. 1983, SoPh, 82, 67,
doi: 10.1007/BF00145546

Wu, C.-J., Krivova, N. A., Solanki, S. K., & Usoskin, I. G.
2018, A&A, 620, A120,
doi: 10.1051/0004-6361/201832956

Yeo, K. L., Krivova, N. A., & Solanki, S. K. 2014, SSRv,
186, 137, doi: 10.1007/s11214-014-0061-7

—. 2017, Journal of Geophysical Research (Space Physics),
122, 3888, doi: 10.1002/2016JA023733

Yeo, K. L., Solanki, S. K., Krivova, N. A., et al. 2020,
Geophys. Res. Lett., 47, e90243,
doi: 10.1029/2020GL090243

Zolotova, N., & Ponyavin, I. 2015, ApJ, 800, 42,
doi: 10.1088/0004-637X/800/1/42